

# A Letter-of-Intent to Jefferson Lab PAC52

## Measurement of the Two-Photon Exchange Contribution to the Positron-Neutron Elastic Scattering Cross Section

S. Alsalmi (spokesperson)

*King Saud University, Riyadh 11451, Saudi Arabia*

E. Fuchey (spokesperson)

*University of Connecticut, Storrs, Connecticut 06269, USA*

(Dated: April 7, 2024)

(\* - TBC)

## Abstract

We propose to make a high precision measurement of the two-photon exchange contribution (TPE) in elastic positron-neutron scattering at two four-momentum transfers  $Q^2$  of 3.0 and 4.5  $GeV^2$ . This measurement purports to complete and extend the measurement of the two-photon exchange in electron-neutron scattering submitted to and approved by PAC48 in 2020, and recorded in 2022 (experiment E12-20-010, currently under analysis), which was the first experiment to examine the impact of the TPE in the neutron form factors experimentally. This program means to address the open question of the discrepancy between GE /GM ratios measured in elastic electron-nucleon scattering via Rosenbluth separation on the one-hand and polarization transfer on the other hand, with the former known to be sensitive to the TPE contribution while the latter isn't. The comparison between the Rosenbluth slope in the positron-neutron measured by the proposed experiment and the Rosenbluth slope in electron-neutron measured by E12-20-010 will provide significant insight on the TPE contribution in the neutron form factors, completing the efforts of MUSE at PSI and the proposed E12+23-008 to measure the TPE contribution on the proton form factors.

The proposed experiment shall be performed in Hall A and will measure simultaneous positron-proton and positron-neutron scattering off deuterium, extracting the Rosenbluth slope of positron-neutron quasi-elastic scattering at two beam energies of 3.3 and 4.4 GeV for  $Q^2 = 3.0\ GeV^2$ , and 4.4 and 6.6 GeV for  $Q^2 = 4.5\ GeV^2$ . In the proposed approach, systematic errors for positron neutron scattering are greatly reduced compared to those in the traditional single arm configuration. The experimental setup of the proposed experiment will be identical to that of the E12-20-010 experiment, using the BigBite (BB) spectrometer to detect the scattered positrons and the Super BigBite Spectrometer (SBS) to detect the protons and neutrons, combined with the proposed positron beam-upgrade for CEBAF. Using the maximum proposed intensity of 1  $\mu$ A unpolarized positrons on 15 cm cryogenic deuterium target, this measurement requires six days on both kinematics. In addition, the measurement requires two extra days with electron beams and 15 cm cryogenic hydrogen target (with 10 A intensity) for calibrations and nucleon detection efficiency measurements, plus two extra days for kinematic change. The analysis of the proposed experiment will

greatly benefit on the return of experience of the ongoing analysis of E12-20-010.

## I. INTRODUCTION

In 1950s, a series of experiments performed by R. Hofstadter [1] revealed that nucleons have a substructure (which corresponds to our modern view in terms of quarks and gluons). The experiment confirmed M. Rosenbluth's theory of electron scattering [2] based on the one-photon exchange approximation. In this so-called Born approximation, where the interaction between the electron and the nucleon occurs *via* an exchange of one virtual photon (OPE), the unpolarized  $e - N$  elastic cross section can be parameterized in terms of a nucleon magnetic,  $G_M$ , and electric,  $G_E$ , form factors. These form factors describe the deviation from a point-like scattering cross section,  $\sigma_{Mott}$ :

$$\left( \frac{d\sigma}{d\Omega} \right)_{eN \rightarrow eN} = \frac{\sigma_{Mott}}{\epsilon(1 + \tau)} [\tau \cdot G_M^2(Q^2) + \epsilon \cdot G_E^2(Q^2)], \quad (1)$$

where  $E$  and  $E'$  are the incident and scattered electron energies, respectively,  $\theta$  is the electron scattering angle,  $\tau \equiv -q^2/4M^2$ , with  $-q^2 \equiv Q^2 = 4EE' \sin(\theta/2)$  being the negative four momentum transfer squared,  $M$  is the nucleon mass, and  $\epsilon = [1 + 2(1 + \tau) \tan^2(\theta/2)]^{-1}$  is the longitudinal polarization of the virtual photon. The reduced cross section is defined by:

$$\sigma_r \equiv \left( \frac{d\sigma}{d\Omega} \right) \cdot \frac{\epsilon(1 + \tau)}{\sigma_{Mott}} = \tau \cdot G_M^2(Q^2) + \epsilon \cdot G_E^2(Q^2) = \sigma_T + \epsilon \cdot \sigma_L, \quad (2)$$

where  $\sigma_L$  and  $\sigma_T$  are the cross sections for longitudinally and transversely polarized virtual photons, respectively.

The linear  $\epsilon$  dependence of the cross section is due to the  $\sigma_L$  term. The ratio  $\sigma_L/\sigma_T$  is the so-called Rosenbluth slope related to  $G_E/G_M$  (in OPE), see Fig. 1. The data show that at  $Q^2$  of 4-5 (GeV/c)<sup>2</sup> the Rosenbluth slope is three to four times larger than expected in OPE (shown as the dot-dashed line in Fig. 1) for the observed values of the  $G_E^p/G_M^p$  ratio.

The nucleon electromagnetic form factors can reveal a lot of information about the nucleon internal structure, as well as the quark distribution. The form factors depend only on one variable, the negative square of the four-momentum transfer carried by the photon,  $Q^2$ . In

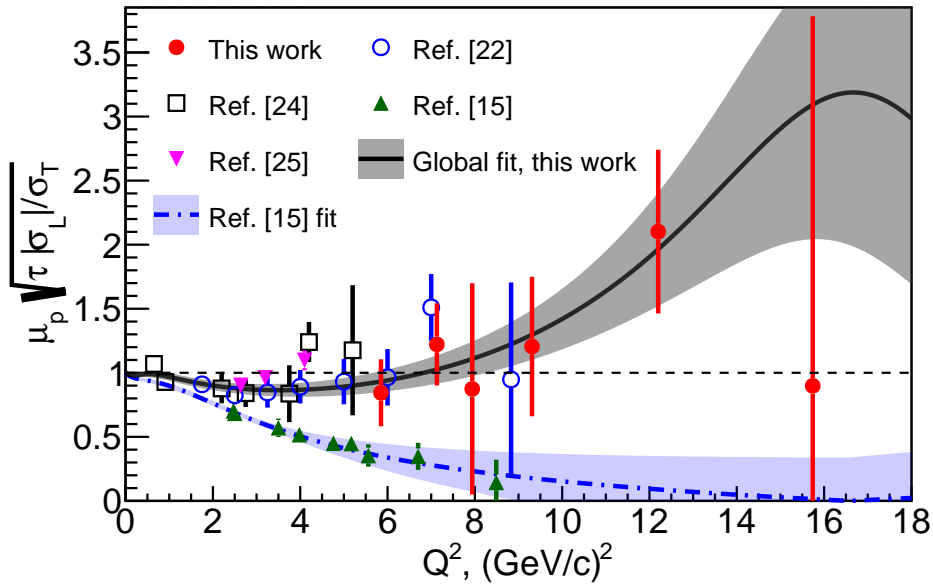


FIG. 1. The square root of Rosenbluth slope, corrected for kinematical factor  $\sqrt{\tau}$  and  $\mu_p$ , observed in elastic electron-proton scattering, adopted from Ref. [3]. References in the plot are also from Ref. [3]

the limit of large  $Q^2$ , perturbative QCD (pQCD) provides well-motivated predictions for the  $Q^2$ -dependence of the form factors and their ratio. However, it was never predicted at what  $Q^2$  range the pQCD prediction (scaling) will be valid. Studies show that pQCD validity will require a very large  $Q^2$  of  $100 \text{ (GeV/c)}^2$ . It was discovered at JLab, using the double polarization methods, that the proton electric and magnetic form factors behave differently starting at  $Q^2 \approx 1 \text{ (GeV/c)}^2$ .

Experimentally, the nucleon form factors can be measured using one of two techniques: the polarization transfer technique and the Rosenbluth technique. The polarization method examines the polarization transfer from longitudinally polarized electron to the recoiling nucleon and determine the resulting azimuthal asymmetry distribution using a polarimeter. Alternatively, one can use a polarized electron beam and polarized target. In the Rosenbluth method, the electric and magnetic form factors can be separated by making two or more measurements with different  $\epsilon$  values (*i.e.* different beam energies and angles), but with same  $Q^2$  value. The Rosenbluth technique requires an accurate measurement of the cross section

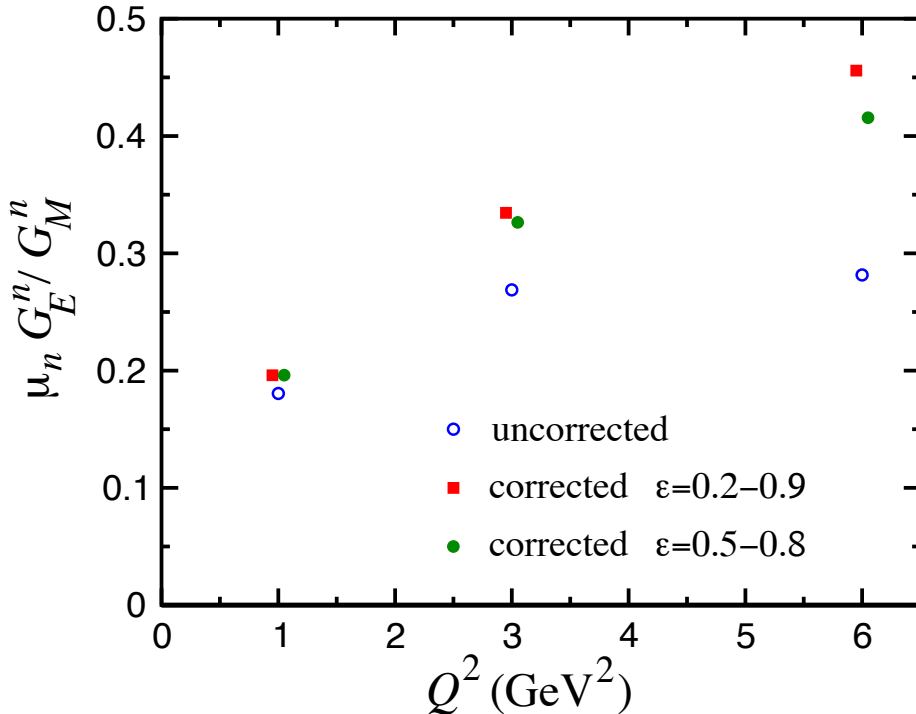


FIG. 2. Projected impact of TPE on  $G_E^n/G_M^n$  using LT separation, according to Ref. [4].

and suffers from large systematic uncertainties arising from several factors, for instance the need for a precise determination of the scattering angle. Additionally, for a measurement of the neutron form factors, accurate knowledge of the neutron detector efficiency is required, which is particularly hard to achieve. These uncertainties can be greatly reduced by measuring the ratio of  $e - n$  and  $e - p$  quasi-elastic cross sections.

When comparing the values of  $G_E^n/G_M^n$  obtained from both techniques, a significant discrepancy was observed (see Fig. 1). Such a discrepancy implies a potential problem in our understanding of the nucleon substructure. Many efforts were made to explain this effect, and it is believed that the inconsistency is due to the contribution of two-photon exchange in  $e - N$  elastic scattering process [5, 6]. Predictions made for the neutron case are shown in Fig. 2, adopted from [4]. The contribution of TPE could reach about 30% of the Rosenbluth slope value at 5 (GeV/c) $^2$ .

50 In the following we propose to make a precision L/T separation of the elastic electron-  
51 neutron cross section and first experimental assessment of the two-photon exchange contribu-  
52 tion on the neutron magnetic form factor measurements (see also Ref. [7]). The result of  
53 the nTPE experiment will likely add a new component to our understanding of the elastic  
54 electron-nucleon process.

55

## II. PHYSICS MOTIVATION

56      The nucleon plays the same central role in hadronic physics that the hydrogen atom does  
 57      in atomic physics and the deuteron in the physics of nuclei. The structure of the nucleon  
 58      and its specific properties, such as charge, magnetic moment, size, mass; the elastic electron  
 59      scattering form factors, resonances; and structure functions in DIS, are of fundamental sci-  
 60      entific interest. The isospin is a fundamental property of the nucleon, so both the proton  
 61      and neutron investigations are important to do. By using data on the proton and neutron  
 62      form factors the flavour structure could be explored [8]. It has already provided the most  
 63      direct evidence for a diquark correlation in the nucleon [9–11].

64      Hadron structure, as seen in elastic electron scattering, in one-photon approximation, is  
 65      defined by two functions of four momentum transfer square. They are: the helicity con-  
 66      serving Dirac form factor,  $F_1$ , which describes the distribution of the electric charge, and  
 67      the helicity non-conserving Pauli form factor,  $F_2$ , which describes the distribution of the  
 68      magnetic moment. These two form factors are the ingredients of the hadronic current. They  
 69      contain information on the transverse charge distribution for an unpolarized and transversely  
 70      polarized nucleon, respectively, in the infinite momentum frame [12, 13].

71      The Sachs form factors,  $G_E$  and  $G_M$ , the ratio of which will be extracted directly from  
 72      the data, are related to  $F_1$  and  $F_2$  by

$$F_1 = \frac{G_E + \tau G_M}{1 + \tau} \text{ and } F_2 = \frac{G_M - G_E}{\kappa(1 + \tau)}, \quad (3)$$

73      where  $\kappa$  is the nucleon anomalous magnetic moment.

74      Already twenty-four years ago, an important development in QCD phenomenology has  
 75      been the exploration of the generalized parton distribution (GPD) formalism [14–16], which  
 76      provides relations between inclusive and exclusive observables. The nucleon elastic form  
 77      factors  $F_1$  and  $F_2$  are given by the first moments of the GPDs

$$F_1(t) = \sum_q \int_0^1 H^q(x, \xi, t, \mu) dx \text{ and } F_2(t) = \sum_q \int_0^1 E^q(x, \xi, t, \mu) dx, \quad (4)$$

78      where  $H^q$  and  $E^q$  are two of the generalized parton distributions,  $x$  is the standard Bjorken  
 79       $x$ ,  $\xi$  is the “skewness” of the reaction,  $t$  is the four-momentum transferred by the electron,

$\mu$  is a scale parameter necessary for the evolution over  $Q^2$ , analogous to DIS parton distributions, and the sum is over all quarks and anti-quarks. GPDs may be accessed through processes such as deeply virtual Compton scattering, where the interaction is factorized into a hard part with the virtual photon/photon interactions with an individual quark and a soft part of the residual system where the GPD information is contained.

A fundamental nucleon feature, the spin, is related to GPDs, as shown by X. Ji [15]. The moments of GPDs can yield information, according to Ji's Angular Momentum Sum Rule, on the contribution to the nucleon spin from quarks and gluons, including both the quark spin and orbital angular momentum.

At present, experimental measurements of GPDs are still scarce. Until high  $Q^2$  DVCS data becomes available, work has been done to attempt to parameterize these GPDs, which rely heavily on data from electromagnetic form factors and parton distributions from DIS as constraints [17]. Data at high  $Q^2$  for  $G_E^n$  would contribute significantly in the development of these models.

As we presented above, nucleon elastic form factors provide important input for the modeling of GPDs. At the same time, the measured cross section of elastic  $e - p$  scattering at high  $Q^2$  is significantly larger than predicted by Born-approximation calculations [18], indicating that TPE effects play a critical role in the high- $Q^2$  region and therefore must be well understood before conclusions about GPDs can be drawn.

99

### III. TECHNIQUE

100 This proposal is based on instrumentation, simulation, and analysis development made  
 101 by the GMn/SBS collaboration for the GMn, E12-09-019, experiment [19]. The GMn experi-  
 102 ment is one of several form factor experiments approved by JLab PAC. The SBS spectrometer  
 103 was funded by DOE with large contributions provided by the collaborating institutions from  
 104 USA, Italy, UK, and Canada. The apparatus and DAQ installation will start in 2020 and  
 105 the data taking run is expected to be in summer-fall 2021.

106 The neutron form factors are challenging to be determine experimentally especially be-  
 107 cause there is no free neutron target. However, since deuterium is a loosely coupled system,  
 108 it can be viewed as the sum of a proton target and a neutron target. In fact, quasi-elastic  
 109 scattering from deuterium has been used to extract the neutron magnetic form factor,  $G_M^n$ ,  
 110 at modestly high  $Q^2$  for decades [20, 21] in the single arm ( $e, e'$ ) experiments. However, the  
 111 proton cross section needs to be subtracted by applying a single-arm quasi-elastic electron-  
 112 proton scattering. This “proton-subtraction” technique suffers from a number of systematic  
 113 uncertainties e.g. contributions from inelastic and secondary scattering processes.

114 Many years ago, L. Durand [22] proposed the so-called “ratio-method” based on the  
 115 measurement of both  $D(e, e'n)$  and  $D(e, e'p)$  reactions. In this method, many of the system-  
 116atic errors are canceled out. Several experiments [23–25] have applied the ratio-method to  
 117 determine the neutron magnetic form factor.

118 The GMn/SBS experiment [19] will take data for elastic  $e - n$  scattering for several  
 119 kinematics with  $Q^2$  from 3.5 up to 13.5  $(\text{GeV}/c)^2$ . We propose to use this method to measure  
 120 the Rosenbluth slope and extract (in OPE approximation) the neutron electric form factor,  
 121  $G_E^n$ , at one value of momentum transfer. In fact, one of the required data points will be taken  
 122 by the GMn experiment, so an additional measurement is needed only for one kinematics.

123 Data will be collected for quasi-elastic electron scattering from deuterium in the process  
 124  $D(e, e'n)p$ . Complementary  $D(e, e'p)n$  data will be taken to calibrate the experiment appa-  
 125 ratus. The current knowledge of the  $e - p$  elastic scattering cross section (obtained in the  
 126 single arm  $H(e, e')p$  and  $H(e, p)e'$  experiments) will be also used for precision determination  
 127 the experiment kinematics.

128 Applying the Rosenbluth technique to measure  $G_E^n$  requires accurate measurement of the  
 129 cross section and suffers from large uncertainties. To overcome this issue, we propose to  
 130 extract the value of  $G_E^n$  from the ratio of quasi-elastic yields,  $R_{n/p}$ , in scattering from a  
 131 deuteron target as follows:

$$R_{n/p} \equiv R_{observed} = \frac{N_{e,e'n}}{N_{e,e'p}} \quad (5)$$

132  $R_{observed}$  needs to be corrected to extract the ratio of e-n/e-p scattering from nucleons:

$$R_{corrected} = f_{corr} \times R_{observed} , \quad (6)$$

133 where the correction factor  $f_{corr}$  takes into account the variation in the hadron efficiencies  
 134 due to changes of the  $e - N$  Jacobian, the radiative corrections, and absorption in path from  
 135 the target to the detector, and small re-scattering correction.

136 In one-photon approximation,  $R_{corrected}$  can be presented as:

$$R_{corrected} = \frac{\sigma_{Mott}^n \cdot (1 + \tau_p)}{\sigma_{Mott}^p \cdot (1 + \tau_n)} \times \frac{\epsilon \sigma_L^n + \sigma_T^n}{\epsilon \sigma_L^p + \sigma_T^p} \quad (7)$$

It is important that the ratio  $R_{Mott} = \frac{\sigma_{Mott}^n \cdot (1 + \tau_p)}{\sigma_{Mott}^p \cdot (1 + \tau_n)}$  could be determine with very high relative accuracy even with modest precision for the beam energy, electron scattering angle, and detector solid angle. Now, let us write the  $R_{corrected}$  at two values of  $\epsilon$  using  $S^{n(p)} = \sigma_L^{n(p)} / \sigma_T^{n(p)}$  as:

$$R_{corrected,\epsilon_1} = \frac{\epsilon_1 \sigma_L^n + \sigma_T^n}{\epsilon_1 \sigma_L^p + \sigma_T^p} \quad R_{corrected,\epsilon_2} = \frac{\epsilon_2 \sigma_L^n + \sigma_T^n}{\epsilon_2 \sigma_L^p + \sigma_T^p}$$

In these two equations there are two unknown variables:  $\sigma_L^n$  and  $\sigma_T^n$ . We remind here that proton and neutron measurements are made simultaneously with the same apparatus. Thanks to this, the dominant contribution to the uncertainty of the Rosenbluth slope of the reduced cross section vs.  $\epsilon$ ,  $S^n = \sigma_L^n / \sigma_T^n$ , will come from the uncertainty of  $S^p$ . At  $Q^2=4.5$  (GeV/c)<sup>2</sup>, according to the global analysis of  $e - p$  cross section [3], the value of  $S^p$  is close to  $1/(\tau \mu_p^2) = 0.087$  with an uncertainty of 0.01. The resulting equation for  $S^n$  is:

$$A = B \times \frac{1 + \epsilon_1 S^n}{1 + \epsilon_2 S^n} \approx B \times (1 + \Delta \epsilon \cdot S^n),$$

<sup>137</sup> with  $\Delta\epsilon = \epsilon_1 - \epsilon_2$ , and where the variable  $A = R_{corrected,\epsilon_1}/R_{corrected,\epsilon_2}$  will be measured  
<sup>138</sup> with statistical precision of 0.1%. Assuming, for this estimate, equal values of  $Q^2$  for two  
<sup>139</sup> kinematics, the  $\tau$  and  $\sigma_T$  for two kinematics are canceled out, and the variable

$$B = (1 + \epsilon_2 S^p)/(1 + \epsilon_1 S^p) \quad (8)$$

<sup>140</sup> For actual small range of  $\epsilon$  and small value of the slope,  $B \approx (1 - \Delta\epsilon \cdot S^p)$ . The value of  
<sup>141</sup>  $B$  will be determined from global proton  $e - p$  data to a precision of  $0.25 \times 0.01$ .

<sup>142</sup> At  $Q^2=4.5$  (GeV/c)<sup>2</sup> the ratio  $\mu_n G_E^n/G_M^n$  is  $0.55 \pm 0.05$  based on polarization transfer data  
<sup>143</sup> which is mostly insensitive to the two-photon exchange, see the 2015 review from Perdrisat  
<sup>144</sup> *et al.* [26]. In the simplest model, the slope  $S^n$  is a sum of the slope due to  $G_E^n/G_M^n$  and the  
<sup>145</sup> neutron two-photon exchange nTPE contribution:

$$S^n = (G_E^n/G_M^n)^2/\tau + \text{nTPE} \quad (9)$$

<sup>146</sup> Without the nTPE contribution, our projected measured slope would be  $S^n = (G_E^n/G_M^n)^2/\tau =$   
<sup>147</sup>  $0.063$ .

<sup>148</sup> If we use the prediction available in [4] which is reproduced on our Fig. 2, nTPE leads  
<sup>149</sup> to increase of the neutron Rosenbluth slope  $S^n$  by a factor 2; Under this assumption, the  
<sup>150</sup> projected measured Rosenbluth slope would now become  $S^n = 0.126$ , and nTPE would then  
<sup>151</sup> be:

$$\text{nTPE} = S^n - (G_E^n/G_M^n)^2/\tau = 0.063. \quad (10)$$

<sup>152</sup> The projected measurement of the neutron two-photon exchange for this experiment is  
<sup>153</sup>  $nTPE = 0.063 \pm 0.012 \pm 0.01$ , where the first uncertainty is due to accuracy of  $G_E^n/G_M^n$  and  
<sup>154</sup> the second one due to projected precision of this experiment. It would be a 4-4.5 sigma  
<sup>155</sup> observation of the two-photon exchange contribution for the neutron.

156

#### IV. PROPOSED MEASUREMENTS

157 We propose to use the same experimental setup of the E12-09-019 experiment. We will  
 158 add a kinematic point at  $Q^2 = 4.5 \text{ (GeV/c)}^2$ , at a higher beam pass (6.6 GeV/3 pass instead  
 159 of 4.4 GeV/2 pass), leading to a higher  $\epsilon$  value. This additional point along with the data  
 160 point of the E12-09-019 experiment will allow us to perform the standard Rosenbluth method  
 161 to obtain (in one-photon approximation) the neutron electric and magnetic form factors. In  
 162 addition, the ratio method (Sec. III), in which the systematic errors are greatly reduced, will  
 163 be implemented to calculate the two photon exchange (TPE) contribution. The study of  
 164 the  $\epsilon$  dependence of the reduced cross section will help examine the two photon exchange  
 165 contribution to the neutron form factor ratio  $G_E^n/G_M^n$ . Table. I displays the kinematic settings  
 166 of the proposed experiment.

Point	$Q^2$ $(\text{GeV}/c)^2$	E (GeV)	$E'$ (GeV)	$\theta_{BB}$ degrees	$\theta_{SBS}$ degrees	$\epsilon$
1	4.5	4.4	2.0	41.88	24.67	0.599
2	4.5	6.6	4.2	23.23	31.2	0.838

TABLE I. Kinematic settings of the proposed experiment. The kinematic point with the lowest  $\epsilon$  value (blue row) is an existing measurement of the approved E12-09-019 experiment.

167

## V. EXPERIMENTAL SETUP

168 As illustrated in Fig. 3, this experiment will study electron scattering from a 15 cm long  
 169 liquid Deuterium target held in a vacuum. The scattered electron will be detected in the  
 170 BigBite spectrometer with an upgraded electron detector stack. The neutron arm is arranged  
 171 with a dipole magnet 48D48 (SBS) and a segmented hadron calorimeter HCAL. The whole  
 172 detector package was designed and is being assembled for the GMn, E12-09-019, experiment.

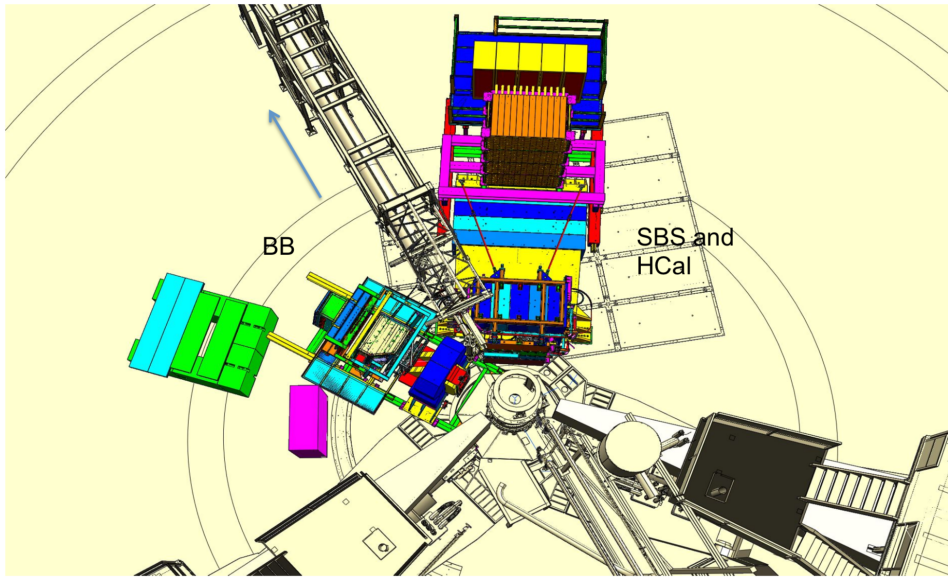


FIG. 3. Layout of the experimental setup in nTPE.

173

### 1. Parameters of the SBS

174 The 48D48 magnet from Brookhaven was acquired as part of the Super Bigbite project  
 175 and will be available for this experiment. It consists of a large dipole magnet which provides  
 176 a field integral of about  $1.7 \text{ T} \cdot \text{m}$ , allowing for quasielastic protons to be sufficiently deflected  
 177 to allow clear differentiation from neutrons. The active field volume has an opening of  $46 \times$   
 178  $25 \text{ vertical} \times \text{horizontal}$ ), matching the aspect ratio of the neutron arm, and a depth of 48  
 179 cm.

180 The placement of this magnet will be 1.6 m away from the target, which would normally

<sup>181</sup> interfere with the beamline. To accommodate this, modifications were made to the iron yoke  
<sup>182</sup> such that the beamline will pass through the magnet yoke area.

<sup>183</sup> The field configuration will be such that positively charged particles will be deflected  
<sup>184</sup> upwards away from the hall floor. For a field integral of 1.7 Tesla-m, protons of momentum  
<sup>185</sup> 2.5 GeV/c will be deflected 250 mrad, which translates to a displacement of 1.29 m. Including  
<sup>186</sup> expected detector resolution, the  $p_{miss,\perp}$  distribution will be similar to what was seen in  
<sup>187</sup> E02-013, so cuts of < 100 MeV/c will be appropriate. Monte Carlo simulations show a  
<sup>188</sup> contamination of charged quasielastics to be negligible.

<sup>189</sup> The presence of the magnet also works to sweep low energy charged particles from the  
<sup>190</sup> target away from the neutron arm. Particles of momentum less than 1.3 GeV/c will be  
<sup>191</sup> entirely swept outside of the neutron arm acceptance. This greatly reduces the amount of  
<sup>192</sup> charged low energy background.

193

### A. The BigBite Spectrometer

194 Scattered electrons will be detected in the BigBite spectrometer. The spectrometer con-  
 195 sists of a single dipole magnet (with magnetic field approximately 1.2 T) and a detection  
 196 system, see Fig. 4.

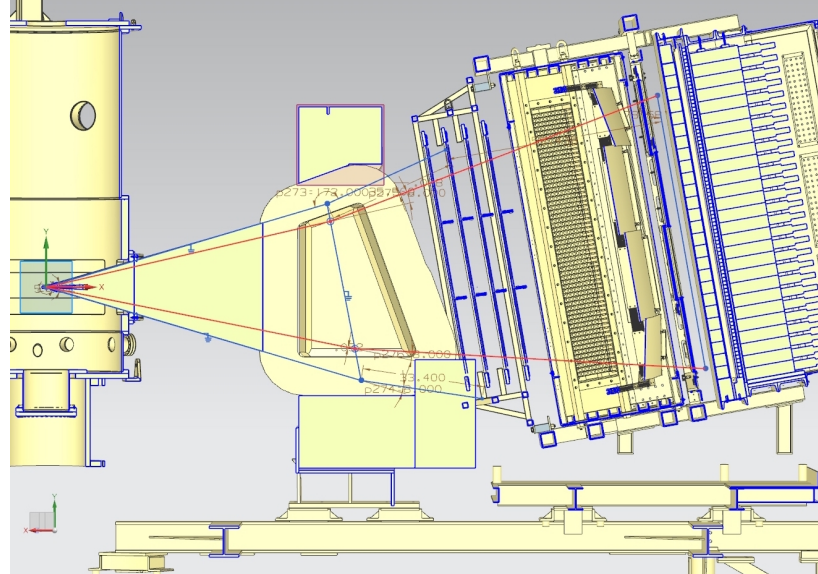


FIG. 4. The BigBite spectrometer with the upgraded detector stack.

197

#### 1. GEM Chambers

198 To perform the tracking of charged particles under the high rates anticipated for this  
 199 experiment, the drift chambers were replaced with gas electron multiplier (GEM) detectors.  
 200 These detectors have proven to be capable of operating under luminosities of  $25 \text{ kHz/mm}^2$   
 201 for the COMPASS experiment at CERN and the spatial resolution of each of these chambers  
 202 is anticipated to be about  $70 \mu\text{m}$ . There will be two sets of GEMs placed on each side of the  
 203 GRINCH Cherenkov detector.

204 The set of GEMs in front of the GRINCH is composed of four layers of GEMs. Two of  
 205 these layers have been built by the SBS collaborators from INFN. They are composed three

206 modules each, measuring  $40 \times 50 \text{ cm}^2$ , such that each layer covers  $40 \times 150 \text{ cm}^2$  (the  
 207 long dimension being vertical, along the dispersive direction). The readout of these modules  
 208 are oriented in the  $x/y$  direction *i.e.* parallel and perpendicular to the dispersive direction  
 209 (horizontal and vertical). The two other layers are being built by the SBS collaborators from  
 210 UVA. They are composed of a single module measuring  $40 \times 150 \text{ cm}^2$ , the long dimension  
 211 again being vertical and along the dispersive direction. The readout of these modules are  
 212 oriented in the  $u/v$  direction *i.e.*  $\pm 30$  degrees with respect to the horizontal direction.

213 The set of GEMs behind the GRINCH has been built by the SBS collaborators from  
 214 UVA. It is composed of a single layer composed of four modules measuring  $50 \times 60 \text{ cm}^2$ ,  
 215 such that the layer covers  $60 \times 200 \text{ cm}^2$  (the long dimension again being along the dispersive  
 216 direction). The readout of these modules are all oriented in the  $x/y$  direction.

217 The background levels in the GEMs have been evaluated, with the help of the G4SBS  
 218 simulation package([27] and Sec. VI) for the  $G_M^n$  experimental readiness review. For the  
 219  $G_M^n$  highest  $Q^2$  point (which is the most constraining, since it combines mandatory maxi-  
 220 mum luminosity and smaller BigBite angles), the rates in the front GEMs are of the order  
 221 of  $120 \text{ kHz/cm}^2$  for the front GEM layers, and below  $50 \text{ kHz/cm}^2$  for the back GEM. To  
 222 perform the GEM tracking within such a high-rate environment, we use the cluster recon-  
 223 structed in the BigBite shower as a track seed to clean the large combinatorics that would  
 224 otherwise be created by the large number of hits. After this, the main challenge is the  
 225 separation by the clustering algorithm of the signal and background hits to minimize track  
 226 smearing. At this level of background, a TreeSearch tracking algorithm combined with a  
 227 fairly simple cluster separation algorithm has already proven to achieve 70% efficiency at  
 228 nominal luminosity. A better cluster separation algorithm is currently being developed and  
 229 should allow to significantly improve this figure.

230

## 2. Shower/Preshower

231 The electromagnetic calorimeter configuration consists of two planes of lead glass blocks  
 232 which we call the preshower and shower. The preshower, located about 80 cm behind the  
 233 first GEM chamber, consists of a  $2 \times 26$  plane of  $37 \text{ cm} \times 9 \text{ cm}$  blocks. The shower, about

<sup>234</sup> 1 m behind the first GEM chamber, consists of an  $7 \times 27$  array of 8.5 cm  $\times$  8.5 cm blocks.  
<sup>235</sup> Sums over these blocks form the physics event trigger for the experiment.

<sup>236</sup> The preshower signal can be used to provide an additional method of pion rejection.  
<sup>237</sup> By selecting low preshower signals, a pion rejection factor of 1:50 can be achieved through  
<sup>238</sup> optimization. Despite higher particle rates, pion rejection performance is anticipated to  
<sup>239</sup> be similar to that achieved for Transversity, E06-010. By measuring the pedestal widths  
<sup>240</sup> and resolution for E06-010 and scaling to this proposal's conditions, overall relative energy  
<sup>241</sup> resolution for the detector is expected to become worse by a factor of 1.6, to about  $\sigma_{\delta E/E} =$   
<sup>242</sup> 25%.

<sup>243</sup> *3. Timing hodoscope*

<sup>244</sup> The BigBite timing hodoscope has been built by the SBS collaborators from Glasgow to  
<sup>245</sup> replace the BigBite scintillator plane. It will be composed of 90 bars stacked in a plane,  
<sup>246</sup> each with dimensions 1 in.  $\times$  1 in.  $\times$  60 cm. The paddle stack will be oriented such that  
<sup>247</sup> the long dimension of the bars is horizontal *i.e.* perpendicular to the dispersive direction.  
<sup>248</sup> Each of these elements are read out by a PMT on each side, mostly to provide measurement  
<sup>249</sup> redundancy.

<sup>250</sup> This plane will primarily be used to provide a signal for nucleon time of flight reconstruc-  
<sup>251</sup> tion. A time resolution of 200 ps is anticipated. This fine segmentation is meant to lower the  
<sup>252</sup> rates in the detector. Background studies made for the  $G_M^n$  experimental readiness review  
<sup>253</sup> demonstrated that the rates experienced by each element was  $\leq$  500 kHz at a luminosity of  
<sup>254</sup>  $2.8 \times 10^{38}$  cm $^{-2}$  s $^{-2}$ . Signals from the PMTs are processed by NINO front-end cards which,  
<sup>255</sup> when the PMT pulse crosses the NINO threshold, will produce a digital signal to be read  
<sup>256</sup> out by CAEN 1190 TDCs which record a leading time and a trailing time.

<sup>257</sup> *4. GRINCH cherenkov detector*

<sup>258</sup> The main purpose of the GRINCH is to provide additional particle identification for offline  
<sup>259</sup> pion rejection. The GRINCH consists of a tank with a maximum depth of 88.9 cm, with 4

260 cylindrical mirrors focusing the cherenkov light directly onto a 510 PMT array (60 lines of  
261 PMTs, with lines of 9 PMTs alternating with lines of 8 PMTs) placed away from the beam.  
262 The radiation gas will be  $C_4F_8$ , which is by far the best compromise between light yield  
263 for electrons and operating cost. With  $n - 1 = 1.35 \times 10^{-3}$ , the  $\pi$  threshold is only about  
264 2.7 GeV, so the additional pion rejection will be most effective below this threshold.

265 Similar to the timing hodoscope, the signals from the GRINCH PMTs pulses are processed  
266 by NINO front-end cards which, when the PMT pulse crosses the NINO threshold, will  
267 produce a digital signal to be readout by VETROC TDCs, which for each PMT hit will  
268 record a leading time and a trailing time. The analog signal will not be recorded however,  
269 which means that for each PMT hit, the information of the number of photoelectrons is not  
270 directly available (although it can in theory be deduced from the time over threshold).

271 All of this implies that the electron selection relies on the number of GRINCH PMT  
272 firing, instead of relying on the signal amplitude.

273

## B. Hadron Calorimeter (HCal)

274

### 1. Description

275 The Hadron Calorimeter (HCal) has been designed specifically to measure the recoil  
 276 nucleon for the SBS experiments. Specifically for this experiment (and for  $G_M^n$ ), HCal  
 277 combined with the SBS (48D48) magnet provides identification of the recoil nucleon, as  
 278 well as additional kinematic constraint and possibly timing information on the measured  
 279 interaction. Nucleon identification is illustrated on Fig. 5. This figure shows the compared  
 280 proton and neutron position distribution in HCal at the same electron kinematics. The  
 281 proton distribution is being shifted upwards by about 1 m compared to the neutron.

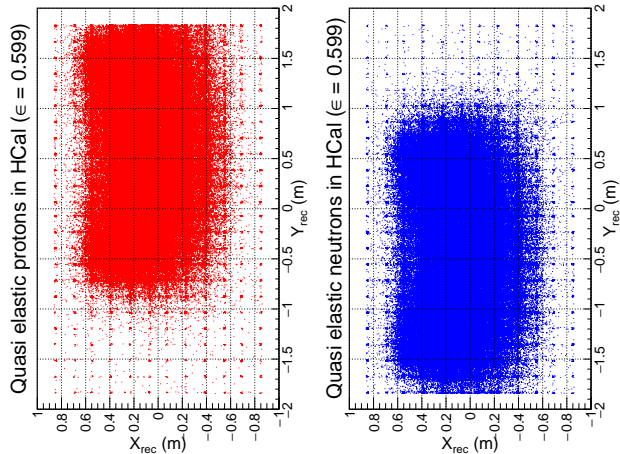


FIG. 5. Reconstructed HCal cluster from quasi-elastic events generated by G4SBS. The left distribution in red is for the proton, the right distribution in blue is for the neutron.

282

The HCal (a CAD model of which is shown in Fig. 6) is composed of 288 modules arranged  
 283 in an array of  $12 \times 24$ . In front of the full assembly is located a  $3/4$  – inch steel plate which  
 285 serves two purposes:

286

- initiate the hadronic shower to optimize the calorimeter response;
- shield the modules from a fraction of the low energy secondaries;

287

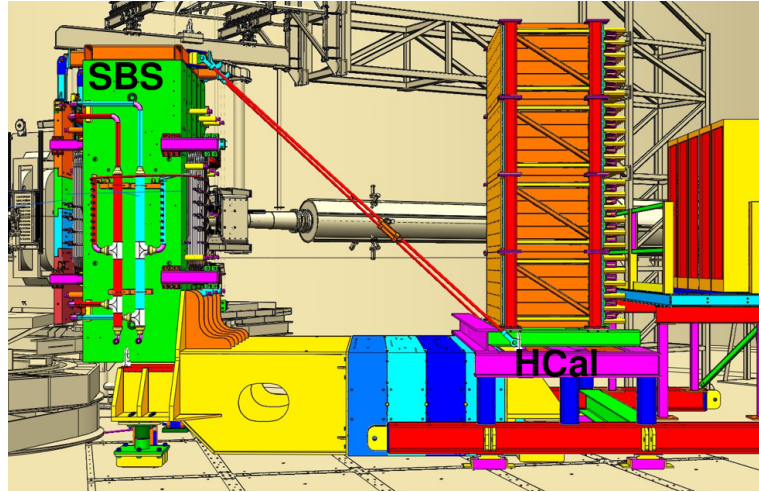


FIG. 6. CAD representation of HCal (right) with the SBS magnet (left)

288 Each of these modules measures  $6 \times 6 \text{ in}^2$  section, for 3 ft length. They are composed of  
 289 alternating tiles of scintillators and iron around a central light guide which collects the light  
 290 generated in the scintillators by the hadronic shower, and guides it to the PMT at the end of  
 291 the block. Cosmic tests have determined that the average light yield for the HCal modules  
 292 is around 5 photoelectrons per MeV deposited in the scintillator tiles.

293 The PMTs are read out with FADC250 which sample the PMT signal every 4 ns and  
 294 allow to reconstruct the PMT pulse shape, and hence its timing. They are also read out by  
 295 TDCs which provide additional timing information. Thanks to this, the timing resolution  
 296 can be better than 1 ns, which cosmic tests (in progress) seem to confirm.

297 The energy resolution is intrinsically broad (see Fig. 12 in Section VI), due mostly to the  
 298 small fraction of energy from the hadronic shower actually measured by the scintillator tiles  
 299 ( $\leq 0.1$  - refer yet again to Fig. 12).

300

## 2. Discussion on HCal efficiency

301 A crucial parameter of this experiment is the hadron calorimeter efficiency, which is  
 302 expected to be slightly different for protons and neutrons, and more importantly the efficiency  
 303 stability.

304      *a. Experimental evaluation of HCal efficiency* The calorimeter efficiency will be mea-  
 305      sured by using "elastic" reactions  $H(e, e)p$ ,  $H(\gamma, \pi^+)n$  and more with  $D(\gamma, \pi^+)n$  and  $D(\gamma, \pi^-)p$   
 306      single pion production. Fig. 7 (a) shows the projected proton position from  $H(e, e)p$ ,  
 307      Fig. 7 (b) shows the projected proton position from  $H(\gamma, \pi^+)n$ . In each case, the trigger will

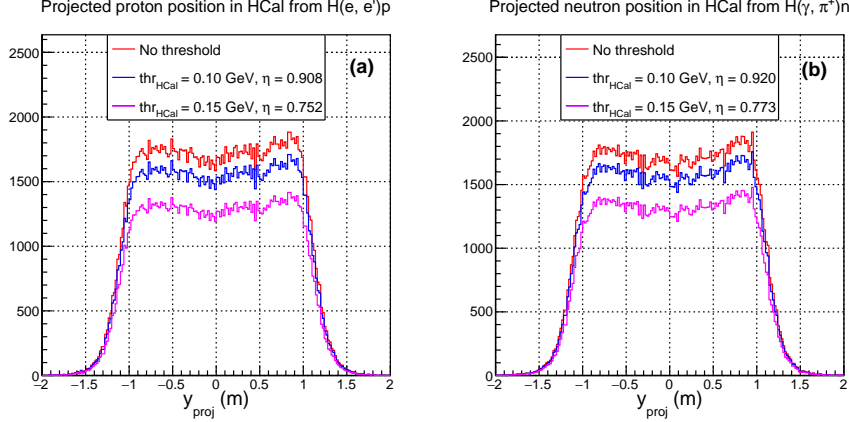


FIG. 7. Projected position in HCal in for the protons in  $H(e, e)p$  (a) and the neutrons in  $H(\gamma, \pi^+)n$  (b). On both panels, red distributions show the projected distribution for  $p, n$ , not detected; blue distributions show the distribution for  $p, n$  detected with a 0.1 GeV threshold; magenta distributions show the distribution for  $p, n$  detected with a 0.15 GeV threshold.

308  
 309  
 310      not use the nucleon detector information. Blue distributions on Fig. 7 show the expected Y  
 311      distribution applying a 0.10 GeV threshold on HCal; Magenta distributions on Fig. 7 show  
 312      the expected Y distribution applying a 0.15 GeV threshold on HCal. As reported in the  
 313      E12-09-019 GMn proposal [19] on Table 8, the expected recorded statistics for  $H(\gamma, \pi^+)n$  are  
 314      of the order of 4000 events, which will represent a relative 1.5% uncertainty on the neutron  
 315      efficiency. The recorded statistics for  $H(e, e)p$  are of the order of 82000 events, which will  
 316      represent a relative 0.3% uncertainty on the proton efficiency.

317

318      *b. Impact of efficiency ratio on the neutron / proton yields ratio*      We want to eval-  
 319      uate the impact of the ratio of hadron efficiencies,

320       $R_{\eta_n/p} = \eta_n/\eta_p$  on the ratio of neutrons to proton yields  $R_{n/p} = N_{en}/N_{ep}$ .

321      To obtain the "true" ratio of neutrons to proton yields  $R_{n/p}$  from the recorded "raw"

<sup>322</sup> ratio of neutrons to proton yields  $R_{n/p,raw}$ , this ratio needs to be corrected by  $R_{n/p}$ .

$$R_{n/p} = R_{n/p,raw}/R_{\eta_{n/p}} \quad (11)$$

<sup>323</sup> Hence, the uncertainty,  $\Delta R_{n/p}$  of  $R_{n/p}$  could be expressed as:

$$\Delta R_{n/p}/R_{n/p} = \Delta R_{\eta_{n/p}}/R_{\eta_{n/p}}. \quad (12)$$

<sup>324</sup> To evaluate the uncertainty of  $R_{\eta_{n/p}} = \eta_p/\eta_n$ , we need to account for the strong correlation  
<sup>325</sup> between  $\eta_p$  and  $\eta_n$ ,  $\rho_{\eta_{n/p}}$ . We can define the covariance between the uncertainties  $\Delta\eta_p$  and  
<sup>326</sup>  $\Delta\eta_n$ ,  $\sigma_{\eta_{n/p}} = \rho_{\eta_{n/p}}\Delta\eta_n\Delta\eta_p$ .

<sup>327</sup> We can write the uncertainty on the ratio efficiencies:

$$\frac{\Delta R_{\eta_{n/p}}}{R_{\eta_{n/p}}} = \sqrt{\left(\frac{\Delta\eta_n}{\eta_n}\right)^2 + \left(\frac{\Delta\eta_p}{\eta_p}\right)^2 - 2\frac{\sigma_{\eta_{n/p}}}{\eta_n\eta_p}} \quad (13)$$

$$= \sqrt{\left(\frac{\Delta\eta_n}{\eta_n}\right)^2 + \left(\frac{\Delta\eta_p}{\eta_p}\right)^2 - 2\frac{\rho_{\eta_{n/p}}\Delta\eta_n\Delta\eta_p}{\eta_n\eta_p}} \quad (14)$$

<sup>328</sup>  $\Delta\eta_p$  and  $\Delta\eta_n$  are the uncertainties from the calibration measurements described above. The

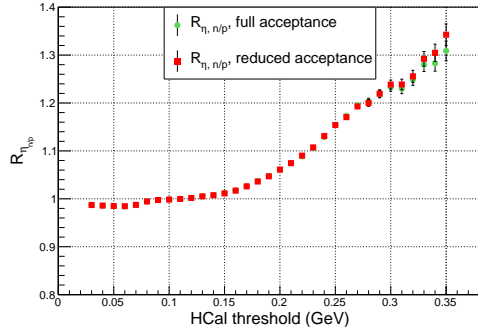


FIG. 8. Neutron/proton efficiency ratio  $R_{\eta_{n/p}}$  as a function of the calorimeter threshold, for our quasi-elastic sample. The error bars represent the uncertainty from the calibration measurements discussed earlier. The green represents  $R_{\eta_{n/p}}$  on the full acceptance, the red represents  $R_{\eta_{n/p}}$  on a reduced acceptance.

<sup>329</sup>

<sup>330</sup>

<sup>331</sup> correlation between the variations of the proton and neutron efficiencies  $\rho_{\eta_{n/p}}$ , depends on

the cause of the variations. In the case of the efficiency calibrations runs, discussed in the Monday write-up, the uncertainties of the efficiencies are due to the statistic of the collected events. In such a case,  $\rho_{\eta_{n/p}} = 0$ . However, in the case of the detector instability,  $\rho_{\eta_{n/p}} \sim 1$  (see again Fig. 8).

With the statistics projected for the calibration runs:  $\eta_p \pm \Delta\eta_p = 0.915 \pm 0.003$  and  $\eta_n \pm \Delta\eta_n = 0.924 \pm 0.014$ . Applying these values to Eq. 14, the relative uncertainty on the absolute value of the hadron efficiency ratio becomes:

$$\Delta R_{\eta_{n/p}}/R_{\eta_{n/p}} = 1.6\%. \quad (15)$$

Considering  $R_{\eta_{n/p}} = 0.991$  from Fig. 8,  $\Delta R_{\eta_{n/p}}/R_{\eta_{n/p}} = 0.016$ . This would add up to the total systematic uncertainty of  $R_{n/p}$  to 1.9% for the low  $\epsilon$  kinematic and to 1.6% for the high  $\epsilon$  kinematic.

342

However, the measurement of the Rosenbluth slope,  $S^n = \sigma_L/\sigma_T$ , is unaffected by the uncertainty of the absolute value of the efficiency ratio  $R_{\eta_{n/p}}$ .  $R_{\eta_{n/p}}$  will be cancelled in the determination of the neutron Rosenbluth slope  $S^n$ , *as long as we control the stability of  $R_{\eta_{n/p}}$  over the few days of the measurement.*

c. *Impact of efficiency stability on the Rosenbluth slope measurement* The specific value of the hadron calorimeter efficiency does not impact the quality of the experimental result. However, the stability of the efficiency ratio is essential.

Let us evaluate in detail the influence of the hadron efficiencies,  $\eta_n$  and  $\eta_p$ , on the experimental result. The  $S^n$  result is sensitive only to the ratio of neutron efficiency to proton efficiency,  $R_\eta = \eta_n/\eta_p$ . Such a ratio is very stable because the nucleon momenta are the same by definition of the Rosenbluth method. We have a plan to monitor the stability of this ratio in our experimental data.

Our primary experimental observable is the ratio of yields  $R_{n/p} = N_{en}/N_{ep}$ . In this experiment, the parameter of interest is  $A = [R_{n/p,\epsilon-1}/R_{n/p,\epsilon-2}] \times [R_{\eta,epsilon-1}/R_{\eta,epsilon-2}]$ .

As we wrote in our proposal, pages 12 and 13, and under the assumption that the reduced

<sup>358</sup> cross section  $\sigma_R$  is linear in  $\epsilon$ , the neutron Rosenbluth slope  $S^n$  can be obtained as:

$$S^n = \frac{A - 1}{\Delta\epsilon} + S^p = \left( \frac{R_{n/p,\epsilon-1}}{R_{n/p,\epsilon-2}} \times \frac{R_{\eta,epsilon-1}}{R_{\eta,epsilon-2}} - 1 \right) / \Delta\epsilon + S^p \quad (16)$$

<sup>359</sup> As it is easy to see from the formula above, the efficiency impact cancels out in  $S^n$  if the  
<sup>360</sup> efficiency ratio is stable.

<sup>361</sup> The procedure to evaluate the hadron detector efficiency was described above. The result  
<sup>362</sup> will be fitted by a few parameter functions, and the ratio of efficiency  $R_\eta$  is characterized  
<sup>363</sup> by those parameters as well as the threshold. This study will be performed for all modules  
<sup>364</sup> of HCal used in the experiment. After the data collection, we will repeat this study with  
<sup>365</sup> the recorded data for each kinematic. Based on projected statistics of a few million events,  
<sup>366</sup> the accuracy of  $R_\eta$  will be better than 0.1%. With such an accuracy, we will monitor the  
<sup>367</sup> stability of  $R_\eta$ . This corresponds to the uncertainty in  $S^n$ , using the formula above, of 0.004,  
<sup>368</sup> with our  $\Delta\epsilon = 0.24$ .

<sup>369</sup> Additional analysis of the efficiency ratio is presented on Fig 8. This analysis focused on  
<sup>370</sup> absolute value of efficiency ratio, for which we expect 1% statistical level. To monitor the  
<sup>371</sup> stability, we will have hundreds of times more statistics.

<sup>372</sup> *d. Efficiency stability due to the detector parameters drift* As we know, the stability  
<sup>373</sup> of the hadron detector efficiency is critical for a successful measurement. The instability of  
<sup>374</sup> the efficiency  $\eta$  over time is mainly due to the drift of the PMTs signals and the related  
<sup>375</sup> electronics. Such an amplitude drift is typically of 1-2% over a few days. It will be better  
<sup>376</sup> for our detector thanks to the LED calibration system.

<sup>377</sup> We expect to use a threshold  $A_{thr} = 100$  MeV (see plots of amplitude spectrum in the  
<sup>378</sup> Monday write-up). Using the graph of the nucleon detection efficiency as a function of the  
<sup>379</sup> threshold  $A_{thr}$  on Fig. 9, we find that, in the region  $A_{thr} = 90 - 110$  MeV, the efficiency is:

$$\eta = 0.92 - 0.18 \times \frac{A[\text{MeV}] - 100}{100} \quad (17)$$

<sup>380</sup> A one percent variation of  $A_{thr}$  leads to 0.2% variation of efficiency.

<sup>382</sup> Turning now to the ratio of efficiencies, we plot it as a function of the threshold on  
<sup>383</sup> Fig. 9. We find that, in the region  $A_{thr} = 90 - 110$  MeV, the ratio of efficiencies is:

$$R_{\eta_n/\eta_p} = \frac{\eta_n}{\eta_p} = 0.998 + 0.011 \times \frac{A[\text{MeV}] - 100}{100}. \quad (18)$$

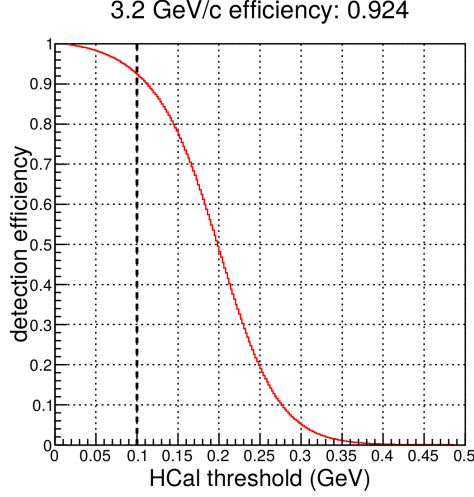


FIG. 9. Nucleon detection efficiency vs the calorimeter threshold  $A_{thr}$ .

- 384 Using the estimate for a PMT-based system instability of 1-2%, which means that  $A_{thr}$  is  
 385 stable to 1-2 MeV, the ratio of efficiencies  $R_{\eta_{n/p}} = \frac{\eta_n}{\eta_p}$  is found to be stable to 0.022%.  
 386 The run plan of the GMn experiment (E12-09-019), which will run next summer, has a  
 387 provision of running on the hydrogen target multiple times with different fields in the SBS  
 388 dipole, allowing the study of the stability of individual modules of HCal.

389      **VI. SIMULATIONS, ESTIMATIONS OF COUNTING RATES AND**  
 390      **ACCIDENTALS**

391      The estimates of counting rates accidentals have been performed using G4SBS, the  
 392      GEANT4-based simulation package developed for the SBS experiment [27]. This package  
 393      includes a wide range of event generators, which allows us to evaluate the rates for both  
 394      events of interest (signal) and background. The representation of the experiment apparatus  
 395      in G4SBS is shown in the high  $\epsilon$  configuration in Fig. 10.

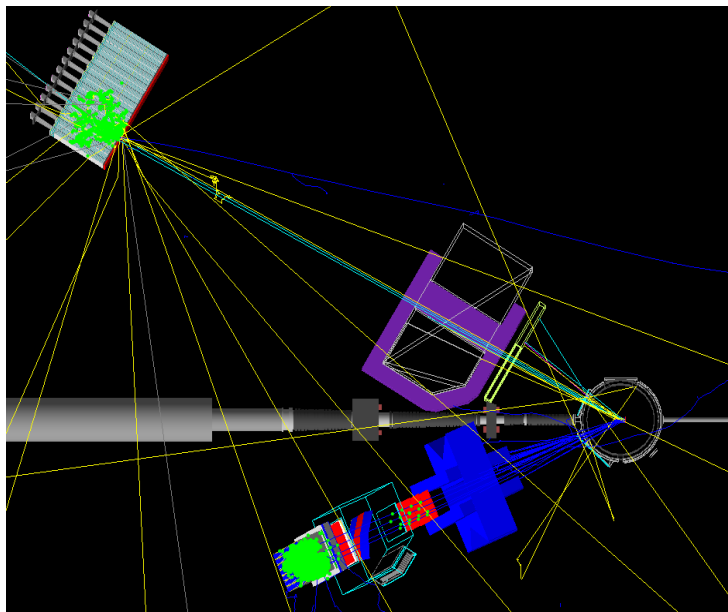


FIG. 10. Top view of the experimental apparatus model in G4SBS, shown in the high  $\epsilon$  configuration. The beam direction is indicated, as well as the main elements (HCal, SBS magnet, BigBite spectrometer)

396      **A. Background and trigger rates**

397      The main processes expected to contribute to the trigger rates for the BigBite spectrom-  
 398      eter are:

- 399      • the inelastic electron nucleon scattering process;

- 400     • photons from inclusive  $\pi^0$  production;

- 401     • and to a lesser extent, charged pions.

402     Concerning HCal, various hadronic backgrounds are expected to contribute to the rates  
 403     in HCal, the dominant ones being pions. Both the inelastic scattering and the inclusive  
 404     neutral and charged pion production are implemented in G4SBS, the latter relying on the  
 405     Wiser parametrization [28]. The minimum-bias “beam-on-target” generator (including all  
 406     electromagnetic and hadronic processes) has also been considered for the HCal background.

407     The thresholds to apply to each arm are determined as a function of the elastic peak. For  
 408     the electron arm, the threshold has been set at  $\mu_E - 2.5\sigma_E$ ,  $\mu_E$  and  $\sigma_E$  being respectively  
 409     the position and width of the fitted elastic peak. Fig. 11 presents the distributions of rate  
 410     of energy deposit for the different processes involved in the BigBite trigger rates.

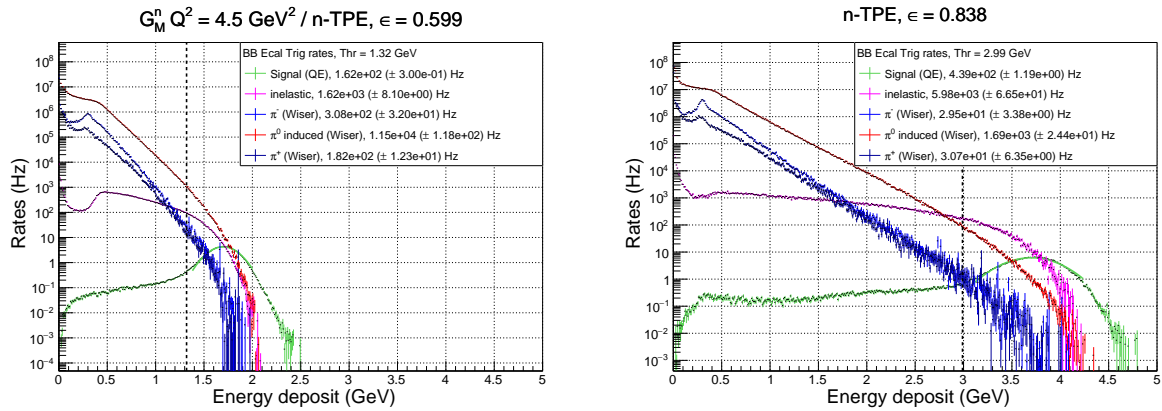


FIG. 11. Rates of the different process contributing to the BigBite electron arm trigger, for the low  $\epsilon$  (left) and the high  $\epsilon$  (right). Quasi-elastic is in green, inelastic in magenta,  $\pi^0$  in red,  $\pi^-$  in blue, and  $\pi^+$  in dark blue. Note the resolution for the elastic peak in the BigBite shower is  $\sim 0.3$  GeV.

411     Since HCal is a sampling calorimeter (meaning that only a fraction of the shower energy  
 412     is measured), its resolution is relatively wide ( $\sim 0.7$  GeV). Due to this, the threshold is at  
 413     90% efficiency (which corresponds to  $\sim 0.1$  GeV for both kinematics. Fig. 12 presents the  
 414     distributions of rate of energy deposit for the different processes involved in the HCal trigger  
 415     rates.

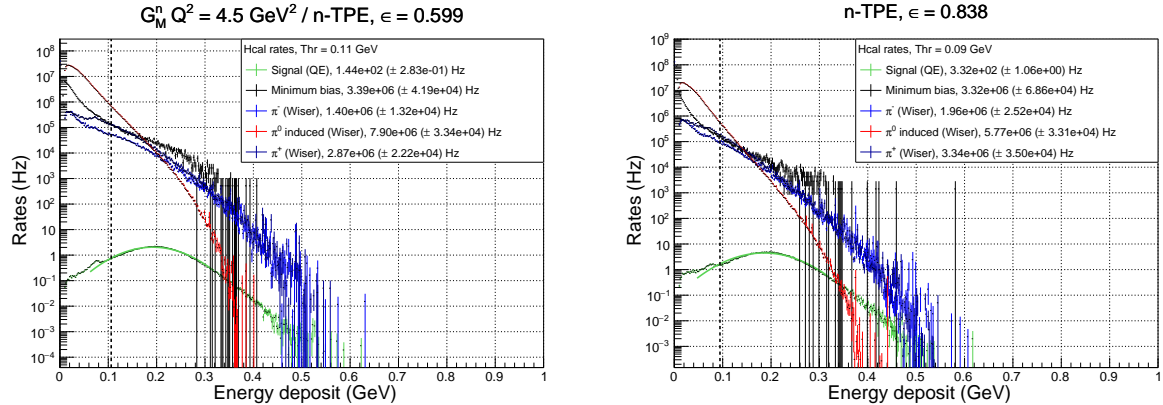


FIG. 12. Rates of the different process contributing to the HCal trigger, for the low  $\epsilon$  (left) and the high  $\epsilon$  (right). Quasi-elastic is in green, minimum bias in black,  $\pi^0$  in red,  $\pi^-$  in blue, and  $\pi^+$  in dark blue. Note the peak itself is around 0.2 GeV for 3.2 GeV nucleons.

417 The thresholds and trigger rates for each arm, as well as the coincidence rate (assuming  
 418 30ns coincidence window), are summarized in Table. II. Note that for HCal, the “total rates”  
 419 is either the “minimum bias” beam on target, *or* the sum of inclusive charged and neutral  
 420 pions evaluated with the Wiser cross sections. Comparisons between Wiser and minimum  
 421 bias at very low energy shows that the Wiser code results dramatically overestimate the  
 422 HCal rates, henceforth the HCal rates estimations using minimum bias are deemed more  
 423 reliable (and emphasized in Table. II). For the sake of thoroughness, we have checked the  
 424 coincidence rates assuming the sum of the inclusive pions (evaluated with the Wiser cross  
 425 sections) as the HCal rates.  
 426

427 *Assuming this worst case scenario*, the coincidence rates could be as high as 5kHz, which  
 428 might be at the limit of manageability for the DAQ. However, even if those rates were proven  
 429 to be accurate, a slight increase on the HCal threshold (which would drop the efficiency from  
 430  $\sim 90\%$  to  $\sim 85\%$ ) would decrease the total HCal rates by  $\sim 35\%$  to 40% in this worst case  
 431 scenario, which would make the situation more manageable (3.3 kHz). In the more reasonable  
 432 case where the HCal rates are more accurately described by the minimum bias prediction,  
 433 the coincidence will be lower than 2kHz, rate at which the SBS DAQ should operate safely.

Point ( $\epsilon$ )	1 (0.599)		2 (0.838)	
	BigBite rates (Hz)	HCal rates (Hz)	BigBite rates (Hz)	HCal rates (Hz)
threshold (GeV)	1.32	0.106	2.99	0.090
Quasi-elastic	$1.62 \times 10^2$	$1.44 \times 10^2$	$4.39 \times 10^2$	$3.48 \times 10^2$
Inelastic	$1.62 \times 10^3$	-	$5.98 \times 10^3$	-
$\pi^-$ (Wiser)	$3.08 \times 10^2$	$1.40 \times 10^6$	$2.95 \times 10^2$	$1.96 \times 10^6$
$\pi^0$ (Wiser)	$1.15 \times 10^4$	$7.90 \times 10^6$	$1.69 \times 10^3$	$5.77 \times 10^6$
$\pi^+$ (Wiser)	$1.82 \times 10^2$	$2.87 \times 10^6$	$3.07 \times 10^2$	$3.34 \times 10^6$
Minimum bias	-	$3.39 \times 10^6$	-	$3.32 \times 10^6$ (*)
<b>Total</b>	$1.37 \times 10^4$	$3.39 \times 10^6$	$8.17 \times 10^3$	$3.32 \times 10^6$
$(\sum_{\pi(Wiser)} \text{for HCal})$		/ $(1.22 \times 10^7)$		/ $(1.11 \times 10^7)$
<b>Coincidence rate</b>	$1.39 \times 10^3$		$8.14 \times 10^2$	
$(\sum_{\pi(Wiser)} \text{for HCal})$	$(5.01 \times 10^3)$		$(2.72 \times 10^3)$	

TABLE II. Trigger rates for BigBite and HCal, with the different process contributions separated, and the sum. For HCal, the total rates is either estimated with the minimum bias generator or the sum of inclusive pions estimated with the Wiser cross section. The coincidence rates assume a 30 ns coincidence window.

434

## B. Contamination from inelastic

435 The main source of contamination for the quasi-elastic comes from the inelastic electron-  
 436 nucleon scattering. Our quasi-elastic  $e - N$  MC generator uses the Kelly form factor fits [].  
 437 Our inelastic resonant  $e - N$  MC generator uses the model by P. Bosted and E. Christy [].  
 438 This model is a fit of  $e - N$  data in the resonance region from Jefferson Lab Hall C [] which  
 439 covers  $0 \leq Q^2 < 8(\text{GeV}/c)^2$ , with beam energies up to 5.5 GeV. According to [], the fit  
 440 residue to the data between 4 and 6 GeV fluctuates by  $\pm 10\%$ . We assume a 20% systematic  
 441 uncertainty on our inelastic cross section.

442 The relevant variables to select the quasi-elastic  $e - N$  scattering from the resonant

<sup>443</sup>  $e - N$  scattering are the missing mass  $W^2 = M_N^2 + 2M_N^2(E - E') - Q^2$ , evaluated with  
<sup>444</sup> the BigBite resolution, of the system  $N(e, e')X$ , and the transverse missing momentum.  
<sup>445</sup> Figure 13 displays the event distributions in  $W^2$  for both our simulated quasi-elastic and  
<sup>446</sup> inelastic samples within the following set of fiducial acceptance cuts:

- <sup>447</sup> • the electron track is reconstructed in BigBite;
- <sup>448</sup> • the total energy deposited in the BigBite calorimeter is above the 3 GeV threshold for  
<sup>449</sup> an average 4.2 GeV elastic peak (for  $\epsilon = 0.84$  kinematic);
- <sup>450</sup> • the electron track must fire at least 3 PMTs in the GRINCH detectors;
- <sup>451</sup> • the total energy deposited in HCal is above the 0.10 GeV threshold. This corresponds  
<sup>452</sup> to 90% efficiency of the 3.2 GeV/c nucleons which deposit 0.20 GeV in the HCal  
<sup>453</sup> (scintillator material).

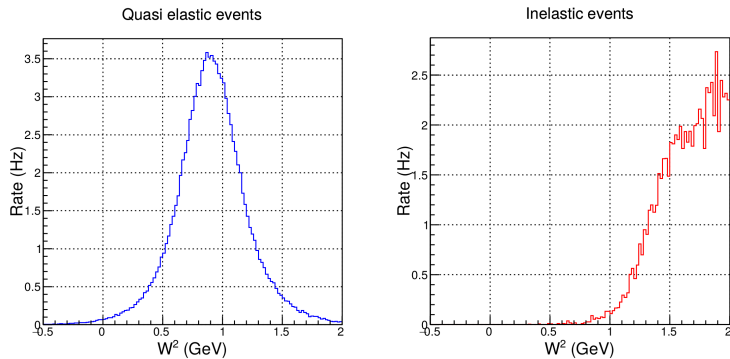


FIG. 13. Event distributions in  $W^2 = M_N^2 + 2M_N^2(E - E') - Q^2$  for quasi elastic  $e - N$  (left) and inelastic resonant  $e - N$  (right) within the fiducial analysis cuts.

<sup>454</sup> Before reconstructing the nucleon momentum, it is necessary to apply a selection cut on  
<sup>455</sup>  $W^2$  to reject a fraction of the inelastic events. To this end, only events for which  $W^2 <$   
<sup>456</sup>  $1.10$  GeV $^2$  are selected for further discussion. Within this selection, our total number of  
<sup>457</sup> events counts 97% of quasi-elastic and 3% of inelastic.

<sup>458</sup> Now we will discuss the missing perpendicular momentum. The nucleon momentum and  
<sup>459</sup> direction is reconstructed using the position of the HCal cluster, on the first step *under*

460 the assumption that it is a neutron. We use the direction of the virtual photon vector  $\vec{q}$   
 461 (corrected with the vertex position) to project the expected neutron position. The difference  
 462 between the reconstructed and the projected nucleon position is shown, projected on  $x$  (the  
 463 non-dispersive direction) and  $y$  (the dispersive direction), for both quasi-elastic and inelastic  
 464 events on figure 14. We clearly distinguish in each case two structures, one which can be

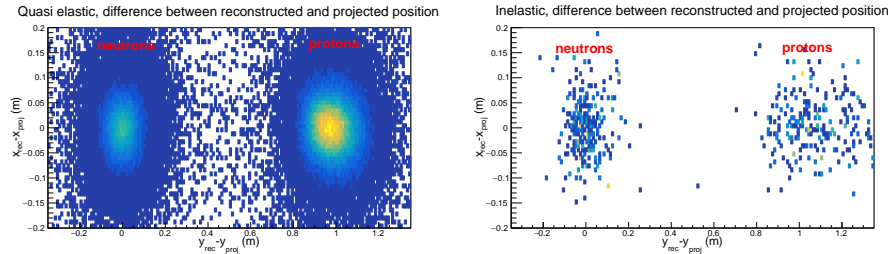


FIG. 14. Difference of projected position and reconstructed position for the nucleons in  $x$  (non-dispersive direction) and  $y$  (dispersive direction), for quasi-elastic events (left) and inelastic events (right). On each plot We clearly notice two structures. The structure on the left, centered at 0, is due to the neutrons. The structure on the right, shifted by about 1 m is due to the protons, which are deflected upwards by the magnetic field.

465  
 466 identified a the neutrons, centered on zero in both  $x$  and  $y$ , and one which can be identified  
 467 as the protons, which are deflected upwards and are shifted by about 1 m in  $y$ . Figure 15  
 468 also shows the difference between the reconstructed and the projected nucleon position,  
 469 except projected on  $y$  (the dispersive direction), for both the quasi-elastic and inelastic  
 470 events. Comparing both the expected inelastic and elastic yields in this variable side-by-side  
 471 evidences further the important role of the  $W^2 < 1.10 \text{ GeV}^2$  selection to filter out inelastic  
 472 events.  
 473

474 As a second step, for the nucleons identified as protons (based on the location of the  
 475 HCal cluster position with respect to its projected position), we need to correct the HCal  
 476 reconstructed position  $y_{rec}$  by the average shift  $\Delta y_{p,avg}$  observed in figure 14 for the nucleons  
 477 identified as protons.  
 478

479 The nucleon momentum norm  $p' = |\vec{p}'|$  is assumed to be equal to the virtual photon norm  
 480  $|\vec{q}|$ . With this information we can calculate the proton shift  $\Delta y_p$  for each proton.

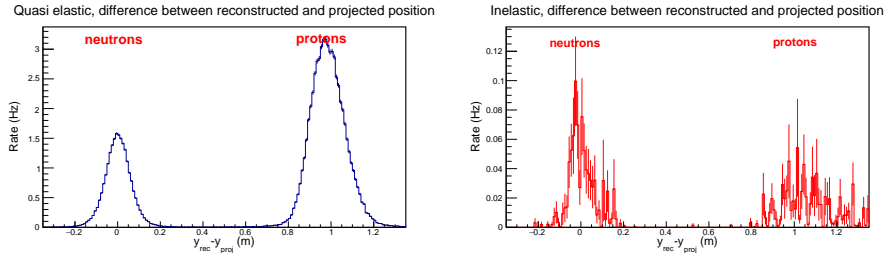


FIG. 15. Difference of projected position and reconstructed position for the nucleons projected in  $y$  (dispersive direction), compared between quasi-elastic (left) and inelastic (right) events. The selection for these distributions are the fiducial cuts  $W^2 < 1.10 \text{ GeV}^2$ . We may notice that the selection on  $W^2 < 1.10 \text{ GeV}^2$  already reduces drastically the proportion of inelastic with respect to quasi elastic. We may also see that the distribution for the proton is slightly wider.

With this information we may build the transverse components of the nucleon momentum (in the SBS coordinates system)  $p'_{x,SBS}$  and  $p'_{y,SBS}$ . For both the protons and neutrons,  $p'_{x,SBS}$  can be written as  $p'_{x,SBS} = p' \times (x_{rec} - v \sin \theta_{SBS}) / (D_{HCal} - v \cos \theta_{SBS})$  (with  $v$  the reconstructed vertex position,  $D_{HCal}$  the HCal distance to the target and  $\theta_{SBS}$  the spectrometer angle. For the neutrons,  $p'_{y,SBS}$  is  $p'_{y,SBS} = p' \times y_{rec} / (D_{HCal} - v \cos \theta_{SBS})$ . For the protons,  $p'_{y,SBS}$  must be written as  $p'_{y,SBS} = p' \times (y_{rec} - \Delta y_p) / (D_{HCal} - v \cos \theta_{SBS})$ .

The nucleon momentum components in the SBS coordinates system  $p'_{x,SBS}$  and  $p'_{y,SBS}$  can then be transformed (using the corrected HCal distance to the target  $D_{HCal} - v \cos \theta_{SBS}$ ) into the nucleon momentum components in the Hall A coordinate system  $p'_x$ ,  $p'_y$  and  $p'_z$ , with the best resolution achievable.

In Hall A coordinate system, using the nucleon meomentum combined with the virtual photon vector  $\vec{q}$ , we may reconstruct the transverse missing momentum  $p_{\perp miss} = \sqrt{(q_x - p'_x)^2 + (q_y - p'_y)^2}$ , which is another very powerful variable to reject more inelastic background. Figure 16 displays the event distributions in  $p_{\perp miss}$  for our simulated quasi-elastic sample within our fiducial acceptance cuts, and requiring  $W^2 < 1.10 \text{ GeV}^2$ . After selection on  $W^2 < 1.10 \text{ GeV}^2$  and  $p_{\perp miss} < 0.1 \text{ GeV}$ , the inelastic contamination of our quasi-elastic sample is better than 1%, with 0.2% systematic uncertainties.

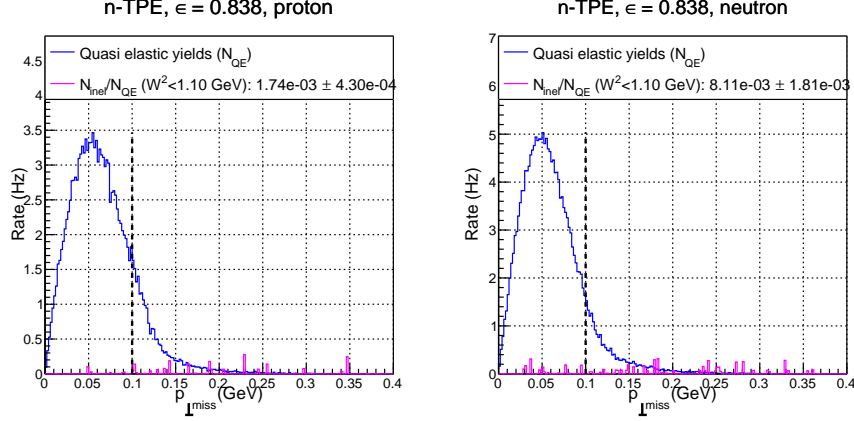


FIG. 16. Compared quasi-elastic (blue) and inelastic (magenta) distributions for  $p_{\perp miss} = \sqrt{(q_x - p'_x)^2 + (q_y - p'_y)^2}$ , within fiducial analysis cuts, after requiring  $W^2 < 1.10 \text{ GeV}^2$ , for the high  $\epsilon$  kinematic, separated between protons on the left and neutrons on the right). The inelastic contamination of quasi-elastic events and their error bars are quoted in the legends.

499

### C. Quasi-elastic counting rates

500 The signals for this experiment have been generated using the G4SBS elastic/quasi-elastic  
 501 generator. We generated a reasonably large sample of quasi-elastic events  $N_{Gen}$  for each  
 502 kinematics, within a solid angle  $\Delta\Omega_{Gen}$  that was larger than the detector acceptance. To  
 503 evaluate the detector solid angle, we define simple criteria that each event has to pass, defined  
 504 as follows:

- 505 • require a primary track, going through all 5 GEM layers (electron arm);
- 506 • require non-zero energy deposit in both the preshower and shower (electron arm);
- 507 • require non-zero energy deposit in HCal (hadron arm).

508 The detector solid angle, for both proton and neutron, are defined in Table. III. We also  
 509 define there the  $p$ - $n$  acceptance asymmetry  $A_{\Delta\Omega}$  such as:

$$A_{\Delta\Omega} = \frac{(\Delta\Omega_e \otimes \Delta\Omega_n) - (\Delta\Omega_e \otimes \Delta\Omega_p)}{(\Delta\Omega_e \otimes \Delta\Omega_n) + (\Delta\Omega_e \otimes \Delta\Omega_p)} \quad (19)$$

Point ( $\epsilon$ )	$\Delta\Omega_e$ (msr)	$\Delta\Omega_e \otimes \Delta\Omega_n$ (msr)	$\Delta\Omega_e \otimes \Delta\Omega_p$ (msr)	$A_{\Delta\Omega}$ (%)
1 (0.599)	52.4	46.7	47.2	0.5
2 (0.838)	32.7	20.8	22.2	3.0

TABLE III. Kinematics electron solid angle, and convoluted electron/hadron solid angle, and acceptance asymmetry.

Then, we evaluate the detection efficiency. For the electron, we require the energy reconstructed in the BigBite calorimeter to be above a threshold defined as  $thr = \mu_E - 2.5 * \sigma_E$ , as well as a minimum number of GRINCH PMTs fired due to the primary electron; For HCal, we select a threshold that yields 90% efficiency. These values are summarized in Table. IV.

Quasi-elastic selection efficiency  $\eta_{sel}$  are also provided.

Point ( $\epsilon$ )	BB thr. (GeV)	HCal thr. (GeV)	$\eta_{det\ e}$	$\eta_{det\ n}$	$\eta_{det\ p}$	$\eta_{sel\ n}$	$\eta_{sel\ p}$
1 (0.599)	1.32	0.11	0.902	0.904	0.892	0.589	0.605
2 (0.838)	2.99	0.09	0.808	0.889	0.882	0.617	0.647

TABLE IV. Kinematics electron thresholds, particle detection efficiencies ( $\eta_{det}$ ), and efficiency of quasi-elastic selection  $\eta_{sel}$  separated for the proton and the neutron.

The counting rates are evaluated using among the  $N_{Gen}$  events generated the events that have passed the selection described below, and weighting those events with the cross section  $d\sigma/d\Omega|_i$  calculated by G4SBS, multiplied by the generation solid angle  $\Delta\Omega_{Gen}$ , using the formula:

$$N_{est} = \frac{\mathcal{L}_{exp}\Delta t}{N_{Gen}} \times \sum_{i \in \text{accepted evts}} \left( \frac{d\sigma}{d\Omega}|_i \times \Delta\Omega_{Gen} \right) , \quad (20)$$

where  $\Delta t$  the running time and  $\mathcal{L}_{exp}$  the experimental luminosity.  $\mathcal{L}_{exp}$  can be calculated as follows:

$$\mathcal{L}_{exp} = \frac{I_{exp}}{q_e} \cdot L_{tgt} \cdot d_{tgt} \frac{\mathcal{N}_A}{m_D} , \quad (21)$$

521 where  $I_{exp}$  is the beam current,  $q_e$  is the electron charge,  $L_{tgt}$  and  $d_{tgt}$  are the target length  
 522 and density respectively,  $N_A$  is Avogadro's number, and  $m_D$  is the deuterium mass number.  
 523 Events are “accepted” if they meet the following criteria:

- 524 • the electron is in the BigBite acceptance;
- 525 • the electron passes the BigBite threshold defined in Table IV and gives signal in the  
 526 GRINCH;
- 527 • the nucleon is in the HCal acceptance and passes the HCal threshold defined in Ta-  
 528 ble IV;
- 529 • the event passes the quasi-elastic selection defined in the previous section *i.e.*  $W^2 \leq 1.1 \text{ GeV}^2$   
 530 and  $p_{\perp miss} \leq 0.10 \text{ GeV}$ .

531 The total quasi-elastic statistics  $N_{QE}$ , as well as the total form factor,  $F^2$ :

$$F^2 = \frac{N_{QE}}{\mathcal{L}_{exp} \cdot \Delta t \cdot d\sigma_{Mott}/d\Omega \cdot \Delta\Omega \cdot \eta} \quad (22)$$

532 and its statistical error  $\Delta F^2 = F^2 / \sqrt{N_{QE}}$  are compiled for both kinematics in Table. VI,  
 533 assuming a running time  $\Delta t = 12$  hours of running at a beam intensity of  $I_{exp} = 30 \mu\text{A}$  on  
 534 a liquid deuterium target with length  $l_{tgt} = 15 \text{ cm}$  and density  $d_{tgt} = 0.169 \text{ g.cm}^{-3}$ . In  
 535 Eq. 13,  $\Delta\Omega$  is the convoluted BigBite-HCal solid angle, and  $\eta$  is the product of all efficiencies  
 536 (detection efficiencies  $\eta_{det} \times$  selection efficiency  $\eta_{sel}$ ).

Point ( $\epsilon$ )	$N_{QE}$ (e-n)	$N_{QE}$ (e-p)	$F_n^2$ ( $\times 10^{-3}$ )	$\Delta F_n^2$ ( $\times 10^{-6}$ )	$F_p^2$ ( $\times 10^{-3}$ )	$\Delta F_p^2$ ( $\times 10^{-6}$ )
1 (0.599)	$9.07 \times 10^5$	$2.55 \times 10^6$	0.99	1.04	2.73	1.70
2 (0.838)	$1.94 \times 10^6$	$5.83 \times 10^6$	0.72	0.52	1.93	0.80

TABLE V. Quasi-elastic counting rates, and total form factor (defined in Eq. 11).

537 The calculation of the  $F_2$  term requires the evaluation of the Mott cross section:

$$\sigma_{Mott} \equiv \frac{d\sigma_{Mott}}{d\Omega} = (\hbar c \alpha_{EM})^2 \frac{1}{4E^2} \left( \frac{\cos \theta_e/2}{\sin^2 \theta_e/2} \right)^2 \frac{E'}{E} \quad (23)$$

<sup>538</sup> The Mott cross section has been calculated with the weighted average of the electron variables  
<sup>539</sup> (momentum and polar angle).

Point ( $\epsilon$ )	$\langle \theta_e \rangle$ (deg)	$\langle k' \rangle$ (GeV)	$\langle Q^2 \rangle$ (GeV $^2$ )	$\sigma_{Mott}$ (nb sr $^{-1}$ )
1 (0.599)	41.88	2.0	4.5	6.62
2 (0.838)	23.23	4.2	4.5	44.2

TABLE VI. The Mott cross section weighted average of kinematic variables over the BigBite acceptance.

540

#### D. Projected results

<sup>542</sup> The projection for our expected Rosenbluth slope measurement is presented on Fig. 17.  
<sup>543</sup> The projected neutron Rosenbluth slope is based on the estimation of the ratio  $\mu_n G_E^n / G_M^n$  at  
<sup>544</sup>  $Q^2 = 4.5$  (GeV/c) $^2$  from the 2015 review from Perdrisat *et al.* [26]. This contribution and its  
<sup>545</sup> uncertainty is represented by the blue dashed curve with the blue dotted area on Fig. 17. To  
<sup>546</sup> this contribution is added the two-photon exchange contribution prediction from [4], which  
<sup>547</sup> projects that the two-photon exchange increases the neutron Rosenbluth slope  $S^n$  by a factor  
<sup>548</sup> 2. The total Rosenbluth slope is shown as the solid magenta curve on Fig. 17. The projected  
<sup>549</sup> uncertainty on our neutron Rosenbluth slope measurement is represented by the solid black  
<sup>550</sup> curve and error bars with the solid red area. The total uncertainty on the two-photon  
<sup>551</sup> exchange contribution is represented by the magenta dotted area on Fig. 17. It is obtained  
<sup>552</sup> combining the projected uncertainty on the neutron Rosenbluth slope measurement with the  
<sup>553</sup> systematic uncertainty on the uncertainty on the ratio  $\mu_n G_E^n / G_M^n$  at  $Q^2 = 4.5$  (GeV/c) $^2$ .

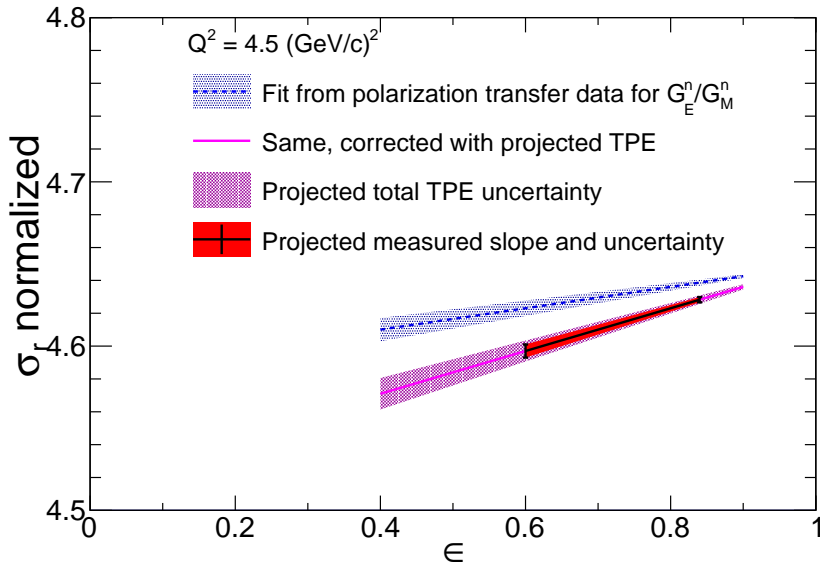


FIG. 17. Projected contribution to the neutron Rosenbluth slope  $S^n$  from  $G_E^n/G_M^n$  (dashed blue curve) with systematic uncertainty (blue dotted area); Total expected neutron Rosenbluth slope  $S^n$  including the expected two-photon exchange (solid magenta). The constraint that our measurement will bring to the slope is represented in solid black with the solid red area. The magenta dotted area shows the total projected uncertainty for nTPE contribution.

554

## VII. SYSTEMATIC ERRORS

555 In this section we will estimate (or set upper limits on) the contributions to the sys-  
 556 tematic uncertainty for this experiment. The sources of systematic uncertainties from the  
 557 experimental setup (target, acceptance, inelastic contamination) were already estimated for  
 558 the SBS  $G_M^n$  experiment proposal [19]. Note that a majority of the potential sources of sys-  
 559 tematic uncertainties (nuclear corrections, accidentals, radiative corrections, target density,  
 560 etc) cancel in the ratio  $R = f_{corr} \times N_{e,e'n}/N_{e,e'p}$ , which is one of the strengths of this experi-  
 561 mental method. The sources of uncertainties as well as their estimation for each kinematic is  
 562 provided in Table. VII. Since the experimental setup has evolved since then, some of these un-  
 563 certainties have been reevaluated, namely the acceptance loss and inelastic contamination.

TABLE VII. Estimated contributions (in percent) to the systematic error on  $R = f_{corr} \times N_{e,e'n}/N_{e,e'p}$ . Quantities marked with \* are taken from the SBS  $G_M^n$  experiment proposal [19]. The total systematic errors on  $R$  is the quadratic sum of all other errors.

Kinematic ( $\epsilon$ )	(1) 0.599	(2) 0.838
Acceptance losses	0.5 %	3.0 %
Inelastic contamination	0.9 %	0.6 %
Nucleon mis-identification*	0.6 %	
Syst. error on $R = f_{corr} \times N_{e,e'n}/N_{e,e'p}$ (Quadratic sum of the errors above)	1.3 %	3.1 %

564

566

567 Table. VII lists the estimated contributions to systematic errors on the two-photon-exchange  
 568 contribution (TPE). The systematics for  $S^p$  and  $\mu_n G_E^n/G_M^n$  have already been explicated in  
 569 Sec. III, and are the leading contributions to the total uncertainty.

570 Inelastic contamination has been reevaluated in Sec. VI B. To evaluate the upper limit on  
 571 our uncertainty, we added quadratically the inelastic contamination evaluated for the proton  
 572 and the neutron for each kinematics. This would be the error that we make on  $R$  if we ignore

TABLE VIII. Estimated contributions to systematic error on the Rosenbluth slope.

Syst. error on $p$ cross section ( $S^p = \sigma_L^p / \sigma_T^p$ )	0.01
Syst. error on $n$ form factor ( $\mu_n G_E^n / G_M^n$ )	0.05
Syst. error on Rosenbluth slope (TPE)	0.012

573 the inelastic contamination in the quasi-elastic  $e - n$  and  $e - p$  samples. Even in this case, we  
 574 expect less than 1% systematic errors. Of course, we do plan to reevaluate and subtract the  
 575 inelastic contamination from our actual data sample, so the quoted systematic uncertainty  
 576 coming from inelastic contamination should be a upper limit.

577 The acceptance loss in SBS (*i.e.* the proportion of non-detected nucleons for each detected  
 578 electron) have been evaluated for both kinematics. They are about 10% for the  $\epsilon = 0.60$   
 579 kinematic (meaning that for every good electron measured, we will not measure the recoil  
 580 nucleon 10% of the times), but they are over 30 % for the  $\epsilon = 0.84$  kinematics, which is due to  
 581 a larger spread of the nucleon imprint. The systematic uncertainty on the acceptance loss for  
 582 the ratio  $R = f_{corr} \times N_{e,e'n} / N_{e,e'p}$  is maximized by the proton-neutron solid angle asymmetry  
 583  $A_{\Delta\Omega} = \Delta\Omega_n - \Delta\Omega_p / \Delta\Omega_n + \Delta\Omega_p$ . This asymmetry is about 0.5% for the  $\epsilon = 0.60$  kinematic  
 584 (consistent with the  $G_M^n$  proposal), but goes up to 3% for the  $\epsilon = 0.84$  kinematics.

585

### VIII. BEAM TIME REQUEST

586     **We request 48 hours total time (32 PAC hours of beam-on target)** to measure  
 587     the two-photon effect (and  $G_E^n$  in one-photon approximation) at  $Q^2 = 4.5$  ( $\text{GeV}/c$ )<sup>2</sup> through  
 588     a measurement of the cross sections of the reaction D(e,e'N) at a large value of the virtual  
 589     photon polarization  $\epsilon=0.84$ . *The measurement at  $Q^2 = 4.5$  ( $\text{GeV}/c$ )<sup>2</sup>,  $\epsilon=0.60$  is already*  
 590     *scheduled as part of the SBS  $G_M^n$  experiment E12-09-019 [19].*

591     We plan to take 12 hours of data at a full luminosity of  $2.86 \times 10^{38} \text{ cm}^{-2}\text{s}^{-1}$ , which  
 592     corresponds to a beam intensity of  $I_{exp} = 30 \mu\text{A}$  on a liquid deuterium target with length  
 593      $l_{tgt} = 15 \text{ cm}$  and density  $d_{tgt} = 0.169 \text{ g.cm}^{-3}$ . To have a better handle on our backgrounds,  
 594     we also plan to take 12 hours of data at half luminosity (basically by lowering the beam  
 595     intensity by a factor 2). In each of these configurations, we also need to take data on a  
 596     “dummy” target (*i.e.* on a target cell identical to the one used for production, but empty)  
 597     to understand the contamination of our data from the target walls.

598     In addition to this beam time, we also require 16 hours (two shifts) to change the exper-  
 599     imental configuration. This configuration change means:

- 600       • BigBite spectrometer angle and distance change;
  - 601       • Beam pass change (from 4.4 GeV/2 pass to 6.6 GeV/3 pass);
- 602     If this experiment is approved, we plan to insert this experiment in the GMn E12-09-019  
 603     run plan in such a way that we can avoid a change in configuration for the SBS magnet  
 604     and the HCal, which is very time consuming. Table. IX displays an excerpt of the GMn run  
 605     plan, and points out where the nTPE measurement inserts. The beam pass change and the  
 606     BigBite move may be done in parallel, and should take one shift (eight hours). We require  
 607     an additional shift (eight hours) for beam tuning after beam pass change. The projected use  
 608     of this time is summarized in Table. X.

611     This experiment will take place in Hall A, along the already scheduled SBS  $G_M^n$  experiment  
 612     E12-09-019, utilizing the BigBite spectrometer to detect electrons scattered off the liquid  
 613     deuterium target, and HCal calorimeter to detect the recoiling neutron and proton.

TABLE IX. Excerpt of GMn E12-09-019 run plan table, showing where the  $\epsilon = 0.84$  measurement would be inserted in our run plan. The  $\epsilon = 0.60$  measurement is also emphasized in blue.

Step #	task	$Q^2$ (GeV/c) <sup>2</sup>	$\theta_{BB} / \theta_{SBS}$ degrees	Beam GeV	Time hours	Tech work time (h)
4b (install GEn-RP)	GEn-RP		41.9 / 24.7	-	4	4
4c (GEn-RP)	Production	4.5	41.9 / 24.7	4.4	104 (calendar) (52 PAC hours)	
4d (remove GEn-RP)	GEn-RP		41.9 / 24.7	-	56	24
<b>4e (GMn/nTPE low <math>\epsilon</math>)</b>	Production	<b>4.5</b>	<b>41.9 / 24.7</b>	<b>4.4</b>	<b>64 (calendar) (32 PAC hours)</b>	
5a (conf. change)	BB/SBS/HCal		32.5 / 31.1	-	32	16
5b (beam tune)	beam		32.5 / 31.1	4.4	4	
5c (GMn)	Production	3.5	32.5 / 31.1	4.4	64 (calender) (32 PAC hours)	
<b>6a (pass change)</b>	beam/BB		<b>23.2 / 31.1</b>	<b>6.6</b>	<b>8</b>	<b>4</b>
<b>6b (beam tune)</b>	beam		<b>23.2 / 31.1</b>	<b>6.6</b>	<b>8</b>	
<b>6c see Table. X</b>	Production	<b>4.5</b>	<b>23.2 / 31.1</b>	<b>6.6</b>	<b>64 (calendar) (32 PAC hours)</b>	
7a (conf. change)	BB/SBS/HCal		58.4 / 17.5		32	16
+ (pass change)	beam		<b>58.4 / 17.5</b>	<b>4.4</b>	during SBS move	
7b (beam tune)	beam	-	58.4 / 17.5	4.4	4	
7c	Production	5.7	58.4 / 17.5	4.4	50 (calendar) (25 PAC hours)	

<sup>614</sup> Data taking (if approved by PAC48) will take place in summer 2021 during the approved  
<sup>615</sup> and scheduled run of the GMn, E12-09-019, experiment, which is going to measure the  $e - n$   
<sup>616</sup> elastic scattering cross section at  $Q^2 = 4.5$  (GeV/c)<sup>2</sup> at  $\epsilon=0.60$ .

<sup>617</sup> The set of instrumentation and required beam current for proposed measurement is iden-

TABLE X. Summary table for the beam time request. Setting changes include SBS and BigBite angles change, as well as a beam pass change from 4.4 GeV (2 pass) to 6.6 GeV (3 pass). This beam pass change can mostly be done in parallel to the SBS

Task	Target	$I_{exp}$	time requested
Data taking (Prod.)	15 cm LD <sub>2</sub>	30 $\mu$ A	12 hours
Data taking (Syst.)	15 cm “Dummy”	30 $\mu$ A	4 hours
Data taking (Prod.)	15 cm LD <sub>2</sub>	15 $\mu$ A	12 hours
Data taking (Syst.)	15 cm “Dummy”	15 $\mu$ A	4 hours
Setting changes (BigBite move, beam pass change)			8 hours
Beam tune after beam pass change			8 hours
<b>Total</b>			<b>48 hours</b>

618 tical to one in the GMn experiment. The beam energy of 6.6 GeV will be used. One of two  
 619 data points required for the cross section LT separation is already in the data taking plan of  
 620 GMn.

621 There are no other measurements of TPE in the  $e - n$  elastic scattering and knowledge  
 622 of the TPE is essential for the understanding of the elastic electron scattering from neutron  
 623 (and proton) and hadron structure. Furthermore, it is a necessary input in the analysis and  
 624 interpretation of a wide range of electron scattering processes.

625 The kinematics of our measurements emphasize the same  $Q^2$  range where TPE in  $e - p$   
 626 elastic scattering was observed to dominate in Rosenbluth slope. Measuring at this high  
 627 momentum transfers will provide unique input for testing TPE calculations [4].

628 We propose to measure the Rosenbluth slope and extract (in one-photon approximation)  
 629  $\delta G_E^n/G_M^n$  to an accuracy of 0.15, which would bring its precision to a level comparable with  
 630 that of the double polarization experiments GEN-RP and GEN-He3 at such value of  $Q^2$ .  
 631 Such precision should be sufficient to detect the TPE contribution to the  $e - n$  Rosenbluth  
 632 slope on the three sigma level.

- 
- 633 [1] R. Hofstadter, *Rev. Mod. Phys.* **28**, 214 (1956).
- 634 [2] M. N. Rosenbluth, *Phys. Rev.* **79**, 615 (1950).
- 635 [3] E. Christy *et al.*, “Two-photon exchange in electron-proton elastic scattering at large four-momentum transfer,” (2020), in preparation for publication in PRL.
- 636
- 637 [4] P. G. Blunden, W. Melnitchouk, and J. A. Tjon, *Phys. Rev.* **C72**, 034612 (2005), arXiv:nucl-th/0506039 [nucl-th].
- 638
- 639 [5] J. Arrington, P. G. Blunden, and W. Melnitchouk, *Prog. Part. Nucl. Phys.* **66**, 782 (2011), arXiv:1105.0951 [nucl-th].
- 640
- 641 [6] A. Afanasev, P. Blunden, D. Hasell, and B. Raue, *Prog. Part. Nucl. Phys.* **95**, 245 (2017), arXiv:1703.03874 [nucl-ex].
- 642
- 643 [7] B. Wojtsekhowski, in *Exclusive processes at high momentum transfer. Proceedings, Newport News, USA, May 15-18, 2002* (2002) arXiv:1706.02747 [physics.ins-det].
- 644
- 645 [8] G. D. Cates, C. W. de Jager, S. Riordan, and B. Wojtsekhowski, *Phys. Rev. Lett.* **106**, 252003 (2011), arXiv:1103.1808 [nucl-ex].
- 646
- 647 [9] C. D. Roberts, M. S. Bhagwat, A. Holl, and S. V. Wright, *Eur. Phys. J. ST* **140**, 53 (2007), arXiv:0802.0217 [nucl-th].
- 648
- 649 [10] J. Segovia, I. C. Cloet, C. D. Roberts, and S. M. Schmidt, *Few Body Syst.* **55**, 1185 (2014), arXiv:1408.2919 [nucl-th].
- 650
- 651 [11] B. Wojtsekhowski (2020) arXiv:2001.02190 [nucl-ex].
- 652 [12] G. A. Miller, *Phys. Rev. Lett.* **99**, 112001 (2007), arXiv:0705.2409 [nucl-th].
- 653 [13] C. E. Carlson and M. Vanderhaeghen, *Phys. Rev. Lett.* **100**, 032004 (2008), arXiv:0710.0835 [hep-ph].
- 654
- 655 [14] D. Muller, D. Robaschik, B. Geyer, F. M. Dittes, and J. Horejsi, *Fortsch. Phys.* **42**, 101 (1994), arXiv:hep-ph/9812448 [hep-ph].
- 656
- 657 [15] X.-D. Ji, *Phys. Rev. Lett.* **78**, 610 (1997), arXiv:hep-ph/9603249 [hep-ph].
- 658 [16] A. V. Radyushkin, *Phys. Lett.* **B380**, 417 (1996), arXiv:hep-ph/9604317 [hep-ph].

- 659 [17] M. Diehl and P. Kroll, *Eur. Phys. J.* **C73**, 2397 (2013), arXiv:1302.4604 [hep-ph].
- 660 [18] N. Kivel, (2020), private communications.
- 661 [19] J. Annand, R. Gilman, B. Quinn, B. Wojtsekhowski, *et al.*, unpublished. See [https://www.jlab.org/exp\\_prog/proposals/09/PR12-09-019.pdf](https://www.jlab.org/exp_prog/proposals/09/PR12-09-019.pdf), [https://www.jlab.org/exp\\_prog/proposals/proposal\\_updates/PR12-09-019\\_pac35.pdf](https://www.jlab.org/exp_prog/proposals/proposal_updates/PR12-09-019_pac35.pdf) (2008).
- 664 [20] E. B. Hughes, T. A. Griffy, M. R. Yearian, and R. Hofstadter, *Phys. Rev.* **139**, B458 (1965).
- 665 [21] R. G. Arnold *et al.*, *Phys. Rev. Lett.* **61**, 806 (1988).
- 666 [22] L. Durand, *Phys. Rev.* **115**, 1020 (1959).
- 667 [23] E. E. W. Bruins *et al.*, *Phys. Rev. Lett.* **75**, 21 (1995).
- 668 [24] G. Kubon *et al.*, *Phys. Lett.* **B524**, 26 (2002), arXiv:nucl-ex/0107016 [nucl-ex].
- 669 [25] J. Lachniet *et al.* (CLAS), *Phys. Rev. Lett.* **102**, 192001 (2009), arXiv:0811.1716 [nucl-ex].
- 670 [26] V. Punjabi, C. F. Perdrisat, M. K. Jones, E. J. Brash, and C. E. Carlson, *Eur. Phys. J.* **A51**, 79 (2015), arXiv:1503.01452 [nucl-ex].
- 672 [27] A. Puckett, unpublished. See [https://hallaweb.jlab.org/wiki/index.php/Documentation\\_of\\_g4sbs](https://hallaweb.jlab.org/wiki/index.php/Documentation_of_g4sbs) (2016).
- 674 [28] D. E. Wiser, “Photoproduction of protons, kaons and pions at slac energies,” Ph.D. thesis,  
675 University of Wisconsin (1977).